Coordinated cerebellar climbing fiber activity is gated by behavioral context in a voluntary motor regime

William Heffley II[1], Eun Young Song[1], Ziye Xu[1], Benjamin Taylor[1], Mary Anne Hughes[1], Andrew McKinney[1,2,3], Mati Joshua[1,4] and Court Hull[1]

[1]Department of Neurobiology, Duke University Medical School, Durham, United States
[2]Neuroscience Department, Baylor College of Medicine, Houston, United States
[3]Duncan Neurological Research Institute at Texas Children's Hospital, Houston, United States
[4]Department of Medical Neurobiology, The Hebrew University, Hadassah Medical School, Jerusalem, Israel

Correspondence:

Dr. Court Hull
Duke University Medical School
Dept. of Neurobiology
311 Research Drive
Durham, NC 27710

Email: Hull@neuro.duke.edu
Phone: 919-613-0927

Acknowledgements:
This work was supported by grants from the NIH NINDS (5R01NS096289-02), the Sloan Foundation, and the Whitehall Foundation. We thank Dr. Lindsey Glickfeld for helpful discussions and input on calcium imaging approaches and analyses, Drs. Stephen Lisberger, Greg Field, Kevin Franks and Fan Wang for feedback on early versions of this manuscript, and members of the Hull and Glickfeld labs for input and technical assistance throughout the project.

Abstract

The prevailing model of cerebellar learning states that climbing fibers (CFs) are both driven by, and serve to correct erroneous motor output. However, this model is grounded largely in studies of reflexive behaviors where CFs respond with high fidelity to the same unconditioned stimuli that evoke erroneous movement. To test whether this model applies to more flexible learning regimes, we have developed a cerebellar-dependent voluntary motor learning paradigm compatible with both mesoscale and single dendrite resolution calcium imaging in mice. Here, we find that CFs are preferentially driven by, and more time-locked to correctly executed movements, exhibiting widespread correlated activity within parasagittal processing zones that depends on behavioral context. Together, these complimentary CF activity patterns are well-suited to drive learning based on successful movement, and suggest that classical supervised learning models must be extended to account for the context-dependent gating of olivary signaling independent from motor errors.

Introduction

A key role of the cerebellum is to form predictive associations between sensory inputs and motor outputs. These sensorimotor predictions are critical for generating well-timed and accurate movements, and in the absence of cerebellar function, the lack of such predictive motor output severely impairs our ability to generate coordinated responses to stimuli in the external world.

Classic models posit that the cerebellum generates sensorimotor predictions according to a supervised learning rule[1-3]. According to such models, projections from the inferior olive called climbing fibers are thought to signal motor errors, thus providing information to Purkinje cells about discrepancies between the expected consequences of a motor command and subsequent sensory feedback. To correct erroneous motor output, the climbing fibers instruct heterosynaptic long-term depression[4-6] by producing powerful regenerative calcium transients[7-9] in Purkinje cell dendrites called complex spikes[10, 11]. In so doing, climbing fibers are thought to appropriately update the cerebellar forward internal model with revised sensorimotor predictions.

This error-signaling framework provides a compelling explanation for climbing fiber activity in a variety of simple behaviors, such as classical conditioning (e.g. eyeblink conditioning) or adaptation (e.g. vestibulo-ocular reflex gain changes)[12-14] paradigms. These behaviors typically make use of an unconditioned stimulus that drives both climbing fibers and the motor response that requires modification. Hence, there is a yoked relationship between sensory input and motor output that allows the climbing fibers to respond with high fidelity to movement error according to the causal association between stimulus and movement.

However, many forms of motor learning do not involve modifications to motor programs driven by an unconditioned stimulus. Instead, the correct association between sensory input and motor output must be learned through experience. Behavioral regimes with such requirements are typically classified under the domain of voluntary motor learning, and cerebellar dysfunction is also known to impair this type of learning[15]. However, it is unclear whether the current model of supervised error signaling can account for either climbing fiber activity or the cerebellar contribution to learning in these more flexible regimes.

To test how the climbing fiber system is engaged under conditions where the sensory and motor signals necessary to drive learning are not innate, we have established a cerebellar-dependent behavioral paradigm compatible with population level *in vivo* calcium imaging, optogenetic and electrophysiological approaches. Using this paradigm, we reveal two key features of cerebellar climbing fiber (CF) driven complex spiking. First, we find that complex spiking cannot be accounted for by a simple error-based supervised learning model. Instead, complex spiking can signal learned, task specific information necessary for flexible control of complex motor behaviors. Second, mesoscale population level recordings reveal that while complex spiking is correlated within and across parasagittal zones, these correlations also depend on behavioral context. While previous measurements have shown increased correlations in complex spiking in response to sensory input or motor output[16-19], and have suggested an important role for synchrony in downstream processing and motor learning[20], our results reveal that such modulation can be contextual, and vary for identical movements depending on behavioral relevance. Hence, these data reveal key features of cerebellar CF activity that differ significantly from classically studied reflexive behaviors, and suggest an extension to current models of complex spiking in order to account for the cerebellar contribution to voluntary motor learning regimes.

Results:

To determine the conditions under which climbing fiber driven complex spiking occurs during a voluntary motor learning regime, we first designed an appropriate sensorimotor learning task. An important feature of the task design is to specifically engage neurons near the dorsal surface of the cerebellum, thereby allowing for visualization of complex spikes at the population level via calcium imaging. Hence, we used optogenetics to functionally map the dorsomedial surface of the mouse cerebellum according to the motor output produced by spatially defined populations of Purkinje cells (PCs). To do so, we expressed Archaerhodopsin (Arch) using a transgenic approach (methods) in cerebellar PCs (Fig. 1A), and used an external fiber coupled laser to transiently suppress PCs near the dorsal surface of the cerebellum (Fig. 1B). Consistent with previous work[21], we identified a population of superficial PCs in lobule simplex capable of

108 driving ipsilateral arm movements either during optogenetic silencing with Arch or following a brief
109 train of electrical simulation (Fig. 1, Supp. Fig. 1, Supp. movie). *In vivo* single unit recording
110 confirmed that our optogenetic stimulation was effective in silencing superficial PCs at the
111 threshold for driving arm movement (~20 mW) up to a depth of 500 μm (Fig. 1B).
112
113 **A cerebellar dependent voluntary motor learning task**
114 Based on these results, we designed a sensorimotor association task involving forelimb
115 movement, with the rationale that the cerebellar contribution to learning in such a task should
116 necessarily involve the PCs capable of driving such movements. This task contains two discrete
117 phases; one where motor output is reactive ('cue reaction'), and another where motor output
118 becomes predictive with learning ('cue prediction'). In both task variations, head restrained, water
119 deprived mice are trained to self-initiate trials by depressing a lever, and to release the lever in
120 response to a visual cue (Fig. 1C,D).
121 In the cue reaction task, trial-to-trial variability in the timing of the visual cue (Fig. 1E,G-
122 "random cue delay") is imposed to necessitate that mice employ reactive forelimb responses. In
123 this regime, lever release reaction times are reflective of the latency for sensory integration[22] and
124 remain constant throughout each session (ΔRT = 1.1 $\pm$ 9.3 ms, n=26 sessions, 7 mice).
125 In the cue prediction task, the visual cue is presented with the same delay on every trial.
126 In this regime, mice learn to predict the timing of the cue and adjust their motor responses to more
127 closely approximate the time of cue (Fig. 1F,G, ΔRT 500ms cue delay = 154.5 $\pm$ 13.6 ms, n=44
128 sessions, 10 mice). Moreover, learning occurs within a single training session (90 min., 300-600
129 trials), is retained across days (Supp. Fig 2A), and can be extinguished by returning mice to the
130 cue reaction paradigm (Supp. Fig 2C,D). In addition, we find that learning depends on the
131 duration of the cue delay: maximal learning occurs at short cue delays (e.g. 500 ms) and little or
132 no learning occurs for cue delays greater than 1.5 seconds (Fig. 1H; one-way ANOVA, main effect
133 of cue delay, $p = 4.8\times10^{-6}$. Post hoc comparison to cue reaction: 500 ms, $p=1.9\times10^{-11}$, 1 s,
134 $p=8.4\times10^{-11}$, 1.5 s, p=0.359, 2 s, p=0.005). This dependence on a short interval delay is consistent
135 with the temporal characteristics of canonical cerebellar-dependent sensorimotor associative
136 learning[23].
137 To test whether animals adjust the timing or kinematics of their forelimb movement to
138 predict the timing of the visual cue, we measured lever kinematics during a subset of learning
139 sessions. Alignment of the lever trajectory to the onset of the cue revealed that animals altered
140 the time of lever release, releasing the lever sooner in anticipation of the visual cue (Fig. 1I; 20%
141 rise time occurs 116 $\pm$ 18 ms earlier, $p = 1.2\times10^{-5}$, paired t-test). However, despite substantial
142 variability in the kinematics of release (Supp. Fig. 3), independent alignment of both press and
143 release demonstrated that there was no change in movement kinematics across learning

144 sessions (Fig 1I-J; First 1/3 of session 20-80% release rise time= 18.9 ± 0.6 ms, last 1/3 of session
145 = 19.3 ± 0.8 ms; p=0.513, paired t-test), indicating that mice release the lever sooner but with the
146 same kinematics after learning.

147 To test the necessity of the lobule simplex for this learning, we first locally applied lidocaine
148 in order to block spiking in cerebellar cortical neurons, including PCs. However, consistent with
149 the critical tonic inhibition PCs provide to the deep cerebellar nuclei, we observed significant motor
150 deficits including slowed movement, dramatically fewer initiated trials, and dystonic limb
151 contractions (not shown). Thus, this manipulation was not appropriate to define the necessity of
152 lobule simplex in our task.

153 To avoid significant impairment of motor output, we next used a pharmacological
154 manipulation to selectively disrupt excitatory synaptic transmission in lobule simplex without
155 abolishing the spontaneous pacemaking of PCs. For these experiments, we optimized
156 concentrations of the excitatory synaptic transmission blockers NBQX (300 μM), CPP (30 μM)
157 and MCPG (30 μM) to avoid visible impairment of motor output, and then tested this cocktail
158 during behavior. Following local drug application to lobule simplex, mice retained the ability to
159 release the lever in response to the visual cue, maintaining stable kinematics across sessions
160 (Fig. 2A,B) that were not different from control sessions (Fig. 1I,J, and Supp. Fig. 3; Press: control
161 range = 28.97 ± 2.5 ms, NBQX range = 25.33 ± 1.9 ms, p=0.2612; Release: control range = 6.16
162 ± 1.2 ms, NBQX range = 4.13 ± 1.06 ms, p=0.2215, unpaired t-test). These data suggest that
163 motor output was not significantly impaired as a result of this pharmacological manipulation.
164 However, despite stable movement kinematics, learning was severely impaired when the cue was
165 presented with a constant 500 ms delay (Fig 2A,C,D) (NBQX ΔRT with 500 ms cue delay = 48.8
166 ± 26.7, control ΔRT with 500 ms cue delay = 154.5 ± 13.6 ms, ΔRT with cue reaction = 1.1 ± 9.3,
167 unpaired t-test NBQX vs control 500 ms p=4.6×10^{-4}, unpaired t-test NBQX vs control cue reaction
168 p=0.05). Single unit PC recordings during drug application revealed that this manipulation
169 significantly reduced complex spike rates, consistent with a reduction in the amplitude of
170 postsynaptic glutamatergic currents produced by climbing fiber input (control 0.60 ± 0.07 Hz,
171 NBQX/CPP/MCPG 0.27 ± 0.04 Hz, n = 9, p=8.5×10^{-4}, paired t-test, Supp. Fig 4). We also found
172 a modest reduction in simple spiking, consistent with reducing excitatory synaptic input from the
173 mossy fibers and parallel fibers (control 66.8 ± 17.8 Hz, NBQX/CPP/MCPG 45.9 ± 13.0 Hz, n =
174 8, n = 9, p=0.36, paired t-test). Hence, these data support that hypothesis that synaptic
175 transmission in lobule simplex is necessary for predictive sensorimotor learning to occur in the
176 cue reaction phase of our task.
177

178 **Complex spiking is not driven by motor errors in a voluntary motor learning task**

To test how the olivary system is engaged in this behavior, we imaged climbing fiber evoked calcium signals in mice performing the cue reaction phase of our task. In this regime, all sensorimotor signals are in place to drive learned, predictively timed forelimb movements, but no learning can occur due to the variable cue timing (Fig. 1G,H). Hence, we can test what task features drive complex spiking in a stable regime. We began by using a mesoscale, single photon microscope to image populations of PCs virally expressing GCaMP6f (methods). Image segmentation in a subset of experiments with the most superficial GCaMP expression revealed structures consistent in size and shape with PC dendrites in cross section (Supp. Fig. 5). Calcium transients in these structures occurred at 0.5 ± 0.01 Hz, consistent with the baseline rate of complex spiking we measured with single unit electrophysiology (Supp. Fig. 5). These results are also consistent with several *in vivo* calcium imaging studies using a variety of GCaMP variants showing that PC responses are dominated by the large dendritic calcium transients produced by climbing fiber driven complex spikes[16-19, 24-29].

We next identified regions of interest, defined by the expression pattern of GCaMP in each animal, that were restricted to the region within lobule simplex capable of driving ipsilateral arm movements (methods). Consistent with the role of this region in the control of arm movements, we observed task modulated PC calcium transients associated with the timing of lever release (Fig. 3A-B). Surprisingly, when we segregated trials according to outcome, we observed significantly larger calcium transients associated with lever releases when animals correctly released the lever in response to the visual cue as compared to trials where lever release occurred prior to the cue (Correct = 0.156 ± 0.023 $\Delta F/F$; Early = 0.092 ± 0.018 $\Delta F/F$, n=17 sessions, 10 animals, $p=4.60\times10^{-5}$, paired t-test). These enhanced responses were distributed widely across dorsal, superficial lobule simplex, and were consistent across sessions and animals (Fig. 3C). Thus, in this voluntary motor task, our data suggest that complex spikes preferentially encode correctly timed movements, and not motor errors.

There are many differences between the correct and early release trials that could contribute to the observed outcome-dependent difference in complex spiking. One possible difference between trial types could be the kinematics of the forelimb movement. Hence, in a subset of our experiments, we measured movement kinematics by comparing lever trajectories on correct and early release trials (Fig. 4A-B). These data, however, revealed closely matched movement kinematics between correct and early lever release trials (Press: correct = 26.8 ± 1.6 ms, early = 25.1 ± 1.3 ms; Release: correct = 18.9 ± 0.8 ms, early: 22.1 ± 1.5 ms, n=14 sessions).

Another difference between correctly timed and early lever releases is that reward is only delivered on correct trials, and this results in extended licking. Indeed, we find that lick rates were significantly higher and prolonged on correct trials (Fig. 4C; correct = 10.5 ± 0.7 Hz, early = 1.5 ± 0.4 Hz, $p=3.74\times10^{-9}$, paired t-test, n=9 animals, 15 sessions). Moreover, in some recording

215 sessions we observed a late, sustained calcium transient that occurred during licking (Fig. 4D).
216 However, we found no correlation between the early, peak calcium transients and lick rates across
217 trial types (Fig. 4E,F; Correct R^2=0.182, p=0.11; Early R^2=5.97x10^{-5}, p=0.98, ANOVA). Thus, we
218 conclude that the enhanced responses as measured by the early peak calcium transient on
219 correctly timed lever releases are not due to differences in arm movement kinematics or licking,
220 but are instead linked to the context of the movement.
221
222 **Behavioral context gates the probability and synchrony of complex spiking**
223 To investigate the dynamics of complex spiking at the single cell level, we used video-rate
224 two-photon microscopy to image the dendrites of PCs during behavior. Using this approach, we
225 isolated the dendrites of individual PCs [25] (Fig.5, Supp. Fig. 5), and measured both spontaneous
226 and task-evoked calcium transients. As with the single photon imaging experiments, spontaneous
227 calcium transients measured during inter-trial intervals occurred at a rate of 0.6 ± 0.01 Hz,
228 consistent with our electrophysiological measurements of spontaneous complex spiking (Supp.
229 Fig. 5E,F). The two-photon data also replicated the main finding that the mean calcium transients
230 were significantly larger on correct release trials within individual PC dendrites (Correct = 0.110 ±
231 0.004 ΔF/F; Early = 0.032 ± 0.002 ΔF/F, n=962, p=1.65^{-75}, paired t-test) (Fig. 5A,B). Moreover,
232 lever releases that were rewarded but occurred too fast to be responses to the visual cue (reaction
233 times less than 200 ms) produced calcium transients that were significantly smaller than those
234 produced by correct lever release trials ('Too fast' 0.028 ± 0.002 ΔF/F, p=2.78^{-100}, paired t-test)
235 and not significantly different from responses on early release trials (p=0.134). Hence, these data
236 support the analysis in Figure 4 that the enhanced complex spiking on correct trials is not due to
237 licking or reward per se.
238 In addition to larger mean responses across trials, population level analysis revealed that
239 more PCs were driven on correct release trials (Fig 5C). Of the total population of PCs that
240 responded to any lever press or release (962 of 1051), most (87%) PCs exhibited complex spikes
241 on correct release trials, whereas less than half (39%) responded during early lever releases (Fig
242 5D). Approximately half (49%) of PCs exhibited complex spikes in response to lever press. The
243 increased number of active dendrites on correct trials is unlikely to be a thresholding artifact, since
244 there was no significant difference in the average response amplitude of correct-only and
245 correct+early responsive dendrites to correct trials (Correct only 0.126 ± 0.006 ΔF/F, n=489;
246 Correct + Early 0.123 ± 0.007 ΔF/F, n=324, p=0.8 Student's t-test). These data also indicate that
247 the measured increase in number of active dendrites is not due to contamination of fluorescent
248 signals from neighboring dendrites. Hence, these single dendrite measurements explain our
249 single photon results by demonstrating that both more PCs exhibit complex spikes on correct

250 trials, and those dendrites that exhibit complex spikes in response to both trial types have larger
251 mean calcium transients on correct trials.

252 The difference in the average release-evoked response on correct versus early trials may
253 be due to a difference in the amplitude of the calcium transients on each trial. For instance,
254 complex spikes are not "all-or-none" events, and the number of spikelets can vary from event to
255 event[30-32], altering the size of the evoked calcium transient[33]. Thus, we extracted single trial
256 events associated with lever releases across trial types, and compared these with each other and
257 to the spontaneous calcium transients. However, this analysis revealed no significant difference
258 between the amplitude of calcium transients evoked on single trials in response to either correct
259 or incorrect lever releases (Correct 0.279 ± 0.005 ΔF/F n=15,586, Early 0.262± 0.005 ΔF/F
260 n=7,705), and between movement-evoked and spontaneous activity (Spontaneous 0.296 ± 0.004
261 ΔF/F n=239,904) (p=0.3, one-way ANOVA) (Fig. 5E). Thus, if there are variable numbers of
262 evoked spikelets across trials, such differences are not systematically correlated with either trial
263 outcome or task engagement. Moreover, the equivalent amplitude of lever-evoked and
264 spontaneous events suggests that the majority of the measured signal is from calcium influx due
265 to complex spiking, and is not substantially influenced by additional input from the parallel fibers.
266 Indeed, the size and shape of our segmented ROIs is consistent with several studies showing
267 that complex spikes produce a calcium signal throughout the entire PC dendrite[7, 9], whereas
268 parallel fiber calcium signals are much smaller and confined to isolated regions of spiny dendritic
269 branchlets[34-37].

270 To assess how equivalent single event responses can produce larger mean responses on
271 correct trials, we generated a peristimulus time histogram of complex spike events for each trial
272 type aligned to the time of release (Fig. 6A). This analysis revealed a significantly enhanced
273 complex spike rate at the time of lever release for trials when movement was correctly timed (Fig
274 6A,B; correct spike rate=2.31 ± 0.01 Hz, early spike rate= 1.39 ± 0.01 Hz, $p=4.54\times10^{-38}$, n=962,
275 paired t-test). In addition, complex spiking on correct trials in single PC dendrites occurred with
276 shorter latency (Fig 6C; correct latency=30.44 ± 0.98 ms, early latency=45.72 ± 1.02 ms,
277 $p=6.37\times10^{-27}$, n=962, paired t-test) and less temporal jitter across trials (Fig 6D; correct jitter (S.D
278 of latency) =65.91 ± 1.75 S.D., n=2140, early jitter 93.29 ± 0.61 S.D., n=1195, $p=1.07\times10^{-31}$,
279 Student's t-test). These results also suggest the possibility of enhanced synchrony at the
280 population level on correct release trials. Indeed, in some sessions, we measured enhanced
281 population synchrony across dendrites (Fig 6E; 5 out of 20 sessions have significantly elevated
282 synchrony on correct trials, open circles, $p=5.11\times10^{-3}$, Mean across the population is not
283 significant, p=0.1305, paired t-test.). However, in many experiments, we observed no such
284 increase in population synchrony on correct trials. We thus considered the possibility that

enhanced synchrony was location specific, and might obey spatial structure that was not well demarcated at the scale of the field of view in our two-photon experiments.

Context determines correlated population activity at the mesoscale level

To investigate whether correlated complex spiking was manifest at the mesoscale, we returned to single photon imaging and analyzed experiments that exhibited widespread GCaMP expression across superficial lobule simplex (n=5 animals, 7 sessions). Using an unsupervised, iterative pixel-clustering approach[27] (methods), we first assessed correlations between pixels across all trials (Fig. 7A). Despite non-uniform, unpatterned GCaMP expression, this analysis revealed spatial patterns of correlated activity that were organized across parasagittal bands oriented in the rostro-caudal axis. These bands were 221 $\pm$ 15 μm wide on average across 39 measured zones, consistent with previous anatomical and physiological measurements of cerebellar microzones[38, 39]. Hence, these data support the longstanding hypothesis that the anatomical pattern of climbing fiber projections into the cerebellar cortex establishes functionally distinct parasagittal processing modules.

To test how complex spiking is modulated during behavior within and across parasagittal zones, we divided trials according to outcome and analyzed brief epochs surrounding the time of lever release (Fig. 7B). This analysis revealed that activity amongst pixels within a zone exhibited higher correlations for most zones on correct lever release trials as compared to early release trials ($r_{correct}$ = 0.77 $\pm$ 0.01, r_{early} = 0.69 ± 0.017, p = 1.60x10^{-5}, n=39 clusters, paired t-test) (Fig. 7C). Because higher spike rates can cause larger correlations, we tested whether the higher complex spike rates on correct trials could account for the higher correlations. While increased complex spiking did produce larger correlations, early release trials still had weaker correlations than correct release trials across equivalent activity levels as assessed by linear fits to bootstrapped distributions paired from each trial type (methods) (Fig. 7D). Hence, the enhanced correlations on correct trials are not an artifact of enhanced complex spike rates on correct trials. We also found enhanced correlations between neighboring and non-neighboring zones on correct lever release trials (Fig. 7E,F). However, these cross-zone correlations were significantly lower on average than those within zones ($r_{neighboring}$ = 0.69 $\pm$ 0.02, n=31 cluster pairs, p=0.004, $r_{non\text{-}neighboring}$ = 0.64 $\pm$ 0.06, n=50 cluster pairs, p=3.88x10^{-4}, Student's t-test). Hence, these data reveal a precise spatial and temporal organization of climbing fiber activity, with highly correlated complex spiking within parasagittal zones that is task specific, differing for movements with the same kinematics depending on behavioral context.

Discussion

320 We have established a cerebellar-dependent sensorimotor association task that involves
321 PCs near the dorsal surface of lobule simplex. This behavior has several hallmarks of cerebellar
322 learning, including dependence on short delay intervals for establishing the learned sensorimotor
323 association and the requirement for excitatory synaptic transmission in the cerebellar cortex.
324 However, this behavior also differs from most cerebellar dependent learning regimes in that the
325 movement requiring modification is not driven by an unconditioned stimulus. In our regime, the
326 proper association between a neutral visual stimulus and movement must be learned before a
327 cerebellar-dependent sensorimotor timing prediction can be established. By breaking the
328 relationship between the specific motor output involved in learning and the unconditioned
329 stimulus, we have revealed patterns of climbing fiber driven complex spiking that are not
330 consistent with the traditional model of error-based supervised learning.

331 In reflexive associative learning paradigms such as conditioned eye-blink learning, the
332 inferior olive is activated by unconditioned sensory input, even in naïve animals. However, in our
333 regime, the cerebellar contribution to motor learning has different requirements, first necessitating
334 that the olivary system establish responses to instructive sensorimotor input that previously had
335 no behavioral relevance, and then utilizing these responses to guide changes in motor output. An
336 important question arising from this finding is whether the initial learning that produces enhanced
337 complex spiking for correctly timed movements occurs at the level of the olive, or if it is inherited
338 from upstream brain regions such as the neocortex, colliculus, or elsewhere. Hence, future
339 experiments designed to test how olivary neurons can flexibly represent learned, task-specific
340 sensorimotor information will be necessary to reveal the origin of such initial learning.

341 Revealing how climbing fiber activity is learned may also reveal how it is gated. Previous
342 work has demonstrated that climbing fiber activity can be gated during different phases of
343 movement[40]. In particular, olivary neurons show reduced excitability during discrete stages of
344 reaching[41, 42] and locomotion[43-45], and this phenomena has been proposed to involve either
345 nucleo-olivary inhibition[46], or an inhibitory pathway from the external cuneate nucleus that can be
346 activated by the red nucleus[47, 48]. Our results demonstrate a new form of gating, where the same
347 movement produces differential climbing fiber activity depending on behavioral context. While
348 our data do not distinguish whether complex spiking is actively enhanced during correct release
349 trials or suppressed during incorrect lever releases, our expectation is that learning the initial task
350 contingencies establishes an association whereby the cued movement (either through sensory or
351 reward-related circuits) can drive enhanced climbing fiber activity. In turn, both the higher
352 probability of complex spiking and enhanced correlation at the population level are ideally suited
353 to facilitate context-dependent motor learning.

354 At the population level, our mesoscale imaging of cerebellar complex spiking has revealed
355 correlated activity within parasagittal bands of approximately 200 μm. This result provides an

356 expanded view of climbing fiber activity, and is consistent with several studies indicating
357 enhanced synchrony in complex spiking across much smaller areas for PCs oriented in the
358 parasagittal axis[27, 49-51]. As previously mapped by the anatomical projection pattern of climbing
359 fibers[52-54], electrophysiology[39, 55] and two photon imaging[17, 27, 56], these parasagittal zones are
360 typically 100-200 μm wide, and are commonly referred to as 'microzones.' Microzones are also
361 related to overlapping, sometimes larger parasagittal compartments defined by the expression of
362 molecular markers such as Aldolase C, the glutamate transporter EAAT4, and others[56-60].
363 Because PCs across microzones can respond to different sensorimotor input, and have different
364 spiking[61] and synaptic[62] properties, these zones are thought to constitute discrete computational
365 units in the cerebellum.

366 To date, it has remained challenging to test how cerebellar processing is organized within
367 and across microzones *in vivo* during behavior, in large part due to the spatial restrictions imposed
368 electrophysiological and multiphoton imaging approaches. Recent measurements have revealed
369 that within parasagittal bands consistent in size with microzones, complex spiking can become
370 more synchronous during both motor output[19] and sensory input[16, 17, 28]. These observations have
371 lent support to the idea that cerebellar processing is functionally segregated to enable
372 sensorimotor learning by clustering responses of like kind onto nearby PCs that in turn converge
373 onto the same deep cerebellar neurons. Our mesoscale imaging results provide a fundamental
374 extension to this idea by demonstrating that correlated complex spiking within parasagittal zones
375 is not simply enhanced by sensorimotor input, but rather can be enhanced for the same action
376 according to behavioral context. This feature is likely to be essential for the cerebellar climbing
377 fiber system to instruct learning in flexible, voluntary regimes where behavioral context is required
378 for accurate motor performance[63]. Precisely timed spiking across a large population of nearby
379 PCs that receive common parallel fiber input and converge to the same DCN neurons would
380 provide an ideal substrate to maximize the impact of plasticity. However, other notable models
381 could also play a role in learning. In particular, complex spiking can robustly inhibit nuclear
382 neurons[64, 65], and enhanced climbing fiber synchrony would magnify this effect via convergence
383 of simultaneously active PC axons in the DCN[66]. Because synchronous inhibition has been
384 shown to play a key role in synaptic plasticity at nuclear neuron synapses[67, 68], correlated complex
385 spiking across populations of nearby PCs could place the DCN as the central site of learning
386 under such conditions[69].

387 Finally, our data suggest that in certain regimes climbing fibers do not signal erroneous
388 motor output as described by classical models of supervised learning. An alternative to these
389 models has recently emerged, suggesting the possibility that climbing fibers may instead operate
390 according to different learning rule[70]. Specifically, conditioned eyeblink learning data has pointed
391 toward a reinforcement learning rule, where climbing fibers instead signal sensory prediction error

392 in order to instruct motor learning. Interpreted within this context, our results are consistent with
393 the possibility that correctly timed lever releases represent positive prediction errors for a
394 movement that accurately predicts future reward delivery. Hence, future experiments specifically
395 designed to test what learning rules are common across different cerebellar behavioral paradigms
396 will be necessary. For the present, the results described here provide an important new
397 demonstration that complex spiking can signal learned, task specific information necessary for
398 flexible control of complex motor behaviors in a manner that does not depend on motor errors.
399
400
401 **Author Contributions**
402 WH, ES, AM, MJ, and CH designed experiments, WH, ES, AM, BT, MAH, and MJ conducted
403 experiments, WH, ES, ZX, BT, AM, MJ, and CH analyzed data, and CH wrote the manuscript.
404
405 **Figure Legends**
406
407 **Figure 1**. Cerebellar sensorimotor task for head-fixed mice. Ai) Confocal image of a sagittal
408 section from PCP2-Cre x Arch mouse showing expression of the inhibitory opsin Arch in PCs at
409 low (left) and high (right) resolution. ML; molecular layer, PCL; Purkinje cell layer, GCL; granule
410 cell layer. Aii) Schematics of a cranial window implanted over lobule simplex (left) and
411 configuration for optogenetic stimulation (right). Bi) *Left*, representative single unit recording of
412 PC simple spike raster (top) and spike rate histogram (bottom) aligned to onset of Arch activation.
413 *Right*, Location of the stimulation sites that evoked ipsilateral arm movements (green). Bii)
414 Average normalized firing rates from superficial (top) or deep (bottom) PCs at low (left) or high
415 (right) stimulation powers (n=5 mice; 10-20 mW – superficial: n=6 cells; deep: n=5 cells; 30-50
416 mW – superficial: n=10 cells; deep: n=4 cells). Note that the lower powers used to map motor
417 responses were only sufficient to strongly suppress neurons above 500 μm. C) Schematic of
418 configuration of behavioral task. Head-fixed mice were trained to release a lever in response to a
419 visual cue. D) Schematic of trial structure. The delay between lever press and release cue was
420 either randomized (cue reaction) or constant (cue prediction) from trial to trial. E) Average
421 reaction time (from cue onset) as a function of trial number for an example cue reaction session.
422 Each point is the average of 5 trials. F) Same as E, for a cue prediction session. G) Summary of
423 reaction times for all cue prediction sessions with a 0.5 s cue delay (gray; n=44 sessions, 10 mice)
424 and all cue reaction sessions (black; n=26 sessions, 7 mice). Error bars are ±SEM across
425 sessions. H) Average change in reaction time from the beginning to the end of cue prediction and
426 reaction sessions (methods). I) *Top*, average lever kinematic traces from an example 0.5 s cue
427 prediction session aligned to the cue show that lever releases occur sooner in the last 1/3 of trials

428 (black) as compared to the first 1/3 of trials (gray). Shaded area is ±SEM across trials. *Bottom,*
429 same example session as above aligned separately to press and release showing no difference
430 in kinematics from beginning (gray) to end (black) of the session. J) Summary of average lever
431 release times (20-80% rise time) across sessions (n=15 sessions, 4 mice)
432
433 **Figure 2**. Learning requires synaptic transmission in lobule simplex. A) Average lever kinematic
434 traces from an example 0.5 s cue prediction session after application of NBQX (300 μM), CPP
435 (30 μM) and MCPG (30 μM). *Top*, traces aligned separately to press and release showing no
436 difference in kinematics from beginning (blue) to end (black) of the session. *Bottom*, traces
437 aligned to the cue show that lever releases do not occur sooner in the last 1/3 of trials (black) as
438 compared to the first 1/3 of trials (blue). Shaded area is ±SEM across trials. B) Summary of
439 average lever release times (20-80% rise time) across NBQX 0.5s cue prediction sessions (n=10
440 sessions, 6 mice). C) Summary of all 0.5 s cue prediction sessions where NBQX (n=14) CPP
441 (n=14) and MCPG (n=8) were applied locally to LS (blue; n=6 mice) compared to summary of cue
442 reaction sessions (black; replotted from Fig 1G). D) Average change in reaction time from the
443 beginning to the end of NBQX 0.5s cue prediction sessions (blue; n=10 sessions, 6 mice)
444 compared to cue prediction and reaction sessions (replotted from Fig. 1H)
445
446 **Figure 3.** Mesoscale single photon imaging during cue reaction sessions. A) Field of view
447 (images separated by 100 ms) showing the average fractional change in fluorescence aligned to
448 lever release for correct (top) and early (bottom) trials from an example session. B) Average
449 timecourse of fluorescent changes from the experiment in A for correct (left, black) and early trials
450 (left, red), and the subtraction of early from correct trials (right). Error bars are ±SEM across trials.
451 C) Summary of the average peak fluorescent transients for all correct and early trials across
452 sessions (n=10 animals, 17 sessions). Colors represent different animals, and each point
453 represents an imaging session. Note that all points lie below the diagonal. *Inset*, schematic of
454 ROIs for all sessions. Outline color corresponds to mouse from scatter plot, and fill color indicates
455 imaging depth identified by post-hoc histology.
456
457 **Figure 4**. Lever dynamics and licking do not explain differences in complex spiking across trial
458 types. A) Average lever kinematics from a representative cue reaction session for correct (black)
459 and early (red) trials aligned to threshold crossing for both press and release. B) Summary of rise
460 times for press (left) and release (right) on correct and early trials across sessions (n=14 sessions,
461 3 mice). C) Average timecourse of licking for correct (top) and early (bottom) release trials across
462 sessions (n=15 sessions, 9 mice). Error bars are ±SEM across sessions. D) Two example
463 sessions illustrating the relationship between release-evoked calcium transients (black and red

464 lines) and licking (blue bars) for correct (left) and early (right) release trials. E) Summary of the
465 relationship between lick rates and the magnitude of fluorescent transients for correct (black) and
466 early (red) release trials (n= 15 sessions, 9 mice). Error bars are ±SEM across trials. F) Summary
467 of the mean ratio of early and correct trial-evoked peak calcium transient and lick rates for the
468 same sessions in E.
469
470 **Figure 5**. Complex spiking produces larger mean response in individual dendrites and enhanced
471 population responses when movement is correctly timed. A) *Left*, average GCaMP fluorescence
472 from an example 2-photon imaging session (30 Hz acquisition rate). Scale bar = 100 μm. *Middle*,
473 pixel mask of individual PC dendrites extracted from the same session. Right, average calcium
474 responses measured from the highlighted dendrite segregated by trial event. Dotted line
475 represents time of lever press (blue) or lever release (correct: black; early: red). Shaded area is
476 ±SEM across trials. B) Left, average timecourse of calcium response for all significantly
477 responsive dendrites aligned to lever press (blue), or release (correct releases (black), early
478 releases (red), and too-fast releases (green) that occurred < 200 ms following the visual cue; n=
479 11 animals, 20 sessions, 962 dendrites). Shaded area is ±SEM across dendrites. *Middle*,
480 summary scatter plot comparing the average peak amplitude of the calcium transient for each
481 significantly responsive PC dendrite (gray) and the average of all dendrites (red) for correct and
482 early release trials. *Right*, same as middle for correct and too fast release trials. C) Pixel masks
483 of dendrites significantly responsive to lever release on correct trials, lever release on early trials,
484 and lever press for the example session in A. Color map represents average ΔF/F. D) Summary
485 across experiments of the fraction of dendrites responsive to correct lever releases vs early
486 releases (top, left), to only correct or only early releases (top, right), to lever press vs release
487 (bottom, left), and only to press or release (bottom, right). E) *Left,* average amplitude of correct
488 and early release-evoked calcium events across all dendrites normalized to the amplitude of
489 spontaneous calcium events. *Right,* mean spontaneous (gray) and correct (black) and early (red)
490 release lever-evoked calcium events across all responsive dendrites Error bars are ±SEM across
491 cells.
492
493 **Figure 6**. Complex spiking occurs with higher peak rates and greater synchrony when movements
494 are correctly timed. A) Peri-release time histogram of calcium events on correct (black) and early
495 (red) release trials (n= 20 sessions, 11 mice, 962 dendrites). Shaded area is ±SEM across
496 dendrites. B) Summary of average event rate for correct and early releases across sessions.
497 Error bars are ±SEM across dendrites. C) Same as B for average event latency relative to release.
498 D) Summary of average standard deviation (S.D.) across events within single dendrites across
499 trials. Error bars are ±SEM across dendrites. E) Same as D for measurement of S.D. across

500 dendrites within each experiment. Open circles are statistically significant for reduced correct trial
501 jitter across dendrites. Error bars are ±SEM across trials.
502
503 **Figure 7**. Complex spiking is correlated across parasagittal zones, with higher correlations on
504 correct lever releases. A) *Left*, Average GCaMP fluorescence for three example experiments.
505 ROIs from lobule simplex (white boxes) were selected for unsupervised clustering analysis (meta
506 K-means, methods). *Right*, voxels are colored according to cluster identity for each example
507 experiment. M=medial, R=rostral, C=caudal, L=lateral. Note the alignment of the clustered zones
508 along the rostro-caudal axis. B) Within cluster voxel-by-voxel correlations between correct and
509 early lever release trials from an example session in A (bottom) for each of the six identified
510 clusters (yellow). C) Summary of average correlation coefficient for all voxel pairs within an area
511 across experiments for correct and early release trials. (n=5 animals, 7 sessions, 39 clusters).
512 Colors denote clusters from the same session. Error bars are ±SEM across voxel pairs. D)
513 Summary of the relationship between peak ΔF/F and correlation coefficients for correct (black)
514 and early (red) trials. Lines are linear fits to each cluster. E) Same as C for pairs of voxels across
515 neighboring clusters. F) Same as C for pairs of voxels across non-neighboring clusters.
516
517 **Supplemental Figures**
518
519 **Figure 1.** Mapping of motor output driven by Arch and electrical stimulation of superficial
520 cerebellar cortex A) Schematics of the results of Arch stimulation over a grid of sites in lobule
521 simplex (Sim) and Crus I for all five mice. Colors denote outcome of stimulation. B) Same as A
522 for three mice tested with electrical microstimulation.
523
524 **Figure 2**. Retention and extinguishment of learning for cue prediction regime. A) Average
525 reaction times relative to cue for the first (left) and second (right) of sessions where animals
526 performed 0.5 s cue prediction on consecutive training days (n=17 sessions, 5 mice). Error bars
527 are ±SEM across sessions. B) Same as A for 2 s cue prediction sessions (n=10 sessions, 6
528 mice). C) *Left,* example cumulative distributions of reaction times for cue reaction sessions
529 immediately surrounding a cue prediction session (session 0). Trials from the cue prediction
530 session include only the last 1/3 of the session when the animal was anticipating the cue timing.
531 *Right,* summary of distribution skewness across cue reaction sessions immediately surrounding
532 cue prediction sessions. D) Same as A for pairs of 0.5 s prediction sessions separated by 3 or
533 more cue reaction sessions (n=20 sessions, 10 mice).
534

535 **Figure 3**. Performance on cue prediction task in control and NBQX sessions. A-E) Summary
536 across experiments of average percent correct lever releases, baseline reaction time from the
537 visual cue, mean reaction time variance, mean duration to press, number of trials performed, and
538 the duration of behavioral sessions. n=44 0.5 s, n=9 1.0 s, n=6 1.5 s, n=30 2.0 s, n=26 Δt, n=14
539 0.5 s NBQX F_i) Individual (top) and average (bottom) lever trajectories aligned to lever press
540 (left) and release(right) segregated by duration into quartiles for a representative 0.5 s cue
541 prediction session. F_{ii}) Same as F_i for a representative 0.5 s cue prediction session in NBQX. G)
542 Summary of press (left) and release (right) quartiles across experiments for control (top; n=15
543 sessions) and NBQX (bottom; n=14 sessions) experiments. H) Summary of the ratio between
544 press and release ranges (difference between 1st and 4th quartile) for control (black) and NBQX
545 (blue) experiments.
546
547 **Figure 4**. Single unit recordings during NBQX application to LS. Top, summary of complex spike
548 rates in control and after application of NBQX for individual cells (black; n=9 cells, 5 mice) and
549 the average of all cells (red). Error bars are ±SEM across cells. Bottom, same as top for simple
550 spike rates. Note that NBQX strongly reduces complex but not simple spike rates.
551
552 **Figure 5**. Segmentation of PC dendrites from imaging experiments. A) Example mesoscale
553 imaging field of view (left) is segmented to mask individual dendrites (right) used for subsequent
554 single cell analysis. Scale bar = 100 μm. B) Example timecourse of raw fluorescence (top) from
555 the circled dendrite in A showing individual calcium transients identified (gray circles) according
556 to peaks in the first derivative of the fluorescence trace (bottom). C) Same as A for an example
557 two photon field of view. Note that while PC somata are visible (round, top right), image
558 segmentation does not extract activity from these structures. Scale bar = 100 μm. D) Same as B
559 for the experiment in C. E) Top, example time course of a single unit PC recording from an
560 awake mouse illustrating detection of complex spikes (gray circles). Bottom, overlay of individual
561 simple (left) and complex (right) spike waveforms (gray) and the average waveform (black). F)
562 Summary of spike rates across all two photon dendrite imaging sessions (blue; n=1051 dendrites)
563 and single unit recordings (n=11 units).
564
565 **Methods:**
566 Mice
567 All experimental procedures using animals were carried out with the approval of the Duke
568 University Animal Care and Use Committee. All experiments were performed during light cycle
569 using adult mice (>p60) of both sexes, randomly selected from breeding litters. All mice were
570 housed in a vivarium with normal light/dark cycles in cages with 1-5 mice. Imaging experiments

571 were performed using Tg(PCP2-Cre)3555Jdhu mice (Jackson Labs, 010536; n=12). Optogenetic
572 mapping experiments were conducted in PCP2-Cre animals crossed with Ai35(RCL-Arch/GFP)
573 (Jax 012735; n=5 mice). Behavioral experiments where imaging was not performed were
574 conducted in wild type C57BL/6J mice (n=18). We used two exclusion criteria for animals in this
575 study: (1) poor recovery or other health concerns following surgical intervention or (2) missed
576 virus injection, as determined by *in vivo* imaging and post-hoc histological analysis.
577
578 Surgical Procedures
579 3-10 hours prior to surgery, animals received dexamethasone (3mg/kg) and ketoprofen (5mg/kg).
580 Surgical procedures were performed under anesthesia, using an initial dose of ketamine/xylazine
581 (50mg/kg and 5mg/kg) 5 minutes prior to surgery and sustained during surgery with 1.0-2.0%
582 isoflurane. Toe pinches and breathing were used to monitor anesthesia levels throughout
583 surgeries. Body temperature was maintained using a heating pad (TC-1000 CWE Inc.). Custom-
584 made titanium headplates (HE Parmer) were secured to the skull using Metabond (Parkell). For
585 imaging experiments, a 3mm diameter craniotomy was made over the lobule simplex
586 approximately 1.4mm lateral and 2.8mm posterior to lambda, and glass cover slips consisting of
587 two 3mm bonded to a 5mm coverslip (Warner Instruments No. 1) with index matched adhesive
588 (Norland No. 1) were secured in the craniotomy using Metabond. Buprenex (0.05mg/kg) and
589 cefazolin (50mg/kg) were administered following surgery twice a day for two days. Following a
590 minimum of 4 recovery days, animals were water deprived for 3 days, or until body weight
591 stabilized at 85% of initial weight, and were habituated to head restraint (3-5 days) prior to
592 behavioral training.
593 For imaging experiments, the glass cover slip was removed following behavioral training,
594 and mice were injected (WPI UMP3) with AAV1.CAG.Flex.GCaMP6f.WPRE.SV40 (UPenn vector
595 core, titer = 9.40×10^{12} or 7.60×10^{12}). 150 nL virus diluted 1:1-1:5 in ACSF was injected at a rate of
596 30nl/min and a depth of 150 μm at 1-3 sites in dorsal lobule simplex. Imaging was performed
597 beginning 14 days following injection.
598 For in vivo pharmacology experiments, a 3mm craniotomy was performed over lobule
599 simplex of headposted mice, and the dura mater was peeled back at the center of the craniotomy.
600 10uL of combined NBQX (300 μM) and CPP (30 μM) was applied 20 minutes prior to behavioral
601 training. In 8 of 14 experiments, MCPG (30 μM) was also included to block metabotropic
602 glutamate receptors. Because there no significant differences in performance across these two
603 groups, all data were pooled for analysis. During behavior, a second drug application of 10uL was
604 administered 20 and 40 minutes into the task, and depending on the duration of training, a third
605 dose was applied after 1 hour. Craniotomies were subsequently covered with silicone elastomer
606 (WPI, Inc.) prior to returning animals to their home cage.

607

608 Behavior

609 During behavioral training, animals were head-fixed and placed in front of a computer monitor,
610 lever and reward delivery tube. Animals were trained to self-initiate trials by depressing the lever
611 using their right forepaw, and required hold the lever in the down position for up to 5 s on the cue
612 reaction paradigm before performing the cue prediction paradigm. Lever releases within one
613 second of the release cue were rewarded (0.01 M saccharine). Animals used for imaging
614 experiments performed the cue reaction task with a mean peak percent correct of 80.1 ± 2.6%.
615 Behavioral parameters including lever press, lever release and licking were monitored using
616 Mworks (http://mworks-project.org) and custom software written in MATLAB (Mathworks). Licking
617 was measured with electrical contact circuit, and the visual cue was presented as a 90° orientation
618 change from a high contrast vertical grating. Inter-trial intervals ranged from 3 to 5 seconds.

619

620 Calcium Imaging

621 *Wide-field imaging*: Single photon, mesoscale imaging was performed using a customized
622 microscope (Sutter SOM) affixed with a 5x objective (Mitutoyo, 0.14NA) and CMOS camera
623 (Qimaging, Rolera em-c^2). Data were collected at a frame rate of 10Hz, with a field of view of
624 3.5x3.5mm at 1002x1004 pixels.

625

626 *Two-Photon Imaging*: Two-photon imaging was performed with a resonant scanning microscope
627 (Neurolabware) using a 16x water immersion objective (Nikon CFI75 LWD 16xW 0.80NA).
628 Imaging was performed using a polymer to stabilize the immersion solution (MakingCosmetics,
629 0.4% Carbomer 940). A Ti:Sapphire laser tuned to 920nm (Spectra Physics, Mai Tai eHP
630 DeepSee) was raster scanned via a resonant galvanometer (8 kHz, Cambridge Technology) onto
631 the brain at a frame rate of either 30Hz with a field of view of 250 by 500um and 264 by 796 pixels,
632 or 15.5Hz with a field of view of 500 by 500um and 529 by 796 pixels. Data were collected through
633 a green filter (510 ± 42 nm band filter (Semrock)) onto GaAsP photomultipliers (H10770B-40,
634 Hamamatsu) using Scanbox software (Neurolabware). A total of 12 mice were used for imaging
635 experiments (10 mice for wide-field, 11 mice for two-photon, 12 mice total).

636

637 Single Unit Recordings and Optogenetics

638 Acute single unit recordings were performed in awake animals by performing a craniotomy over
639 lobule simplex and inserting a multi-electrode silicone probe (Neuronexus, A4x8-5mm-100-400-
640 177-A32, 4 shanks, 8 site/shank at 100 μm spacing) using a Cerebus multichannel acquisition
641 system (Blackrock Microsystems, Salt Lake City). Continuous recording data was bandpass
642 filtered with a 2-pole Butterworth between 250 Hz and 5 kHz and referenced against an electrode

643 with no spikes using Spike2. Single units were isolated by amplitude thresholding. Template
644 waveforms were defined and characterized by their width and peak, and PCA of waveforms was
645 done in off-line in Spike2.
646 Complex spikes and simple spikes were discriminated as in de Solages et al.[71], first on
647 the basis of their stereotypical waveform. Complex spikes typically had a multi-wavelet form,
648 including a large positive peak within 6ms following spike initiation. Manual identification of 10-
649 20 complex spikes was used to generate a mean template waveform, which was then compared
650 to all other spikes for a given unit using the Spearman rank order correlation coefficient. The
651 combination of Spearman coefficients and the magnitude of the positive waveform deflection was
652 used to segregate complex and simple spikes. The presence of a post-complex spike pause (20
653 ms or more) in simple spike firing was verified by cross-correlogram for all isolated single units.
654
655 Histology
656 Mice were deeply anesthetized with ketamine/xylazine (200mg/kg & 30mg/kg respectively, IP)
657 then perfused with PBS then 4% paraformaldehyde. 100um sagittal sections were cut using a
658 vibratome (Pelco 102). Cerebellar slices were then mounted using a mounting medium (Southern
659 Biotech Fluoromount-G or DAPI Fluoromount-G) and imaged with a fluorescence microscope
660 (Nikon Eclipse 80i).
661
662 Data Analysis
663 *Behavior:* Behavior sessions were only analyzed within the time range of active task
664 performance. Accordingly, the last trial of each session was determined by the occurrence of
665 either two consecutive failed trials (in which the mouse did not release the lever in response to
666 the cue) or two consecutive trials with post-ITI duration to press longer than 1.5x the session
667 average.
668 Reaction times were measured using lever releases within the reward window as well as
669 those occurring 200ms prior to the reward cue to account for predictive responses. Reaction times
670 are plotted as a binned average of five trials. Initial reaction times were calculated according to
671 the y-intercept of the linear regression of the first fifty trials. Final reaction time at the end of each
672 session was calculated by averaging the reaction times of trials 200-250.
673 The symmetry of reaction time data about the sample mean was measured to test the
674 extinguishment of learning after following cue prediction sessions according to skewness.
675 Sample skewness was defined by
676
677 $$s = \frac{E(\mu - X)^3}{\sigma^3}$$

where μ is the mean of X, $E(*)$ is the expected value of the quantity $*$, and σ is the standard deviation of X. Thus for a given sample x, this calculates:

$$\frac{\frac{1}{n}\sum_{i=1}^{n}(x_i - \bar{x})^3}{\left(\sqrt{\frac{1}{n}\sum_{i=1}^{n}(x_i - \bar{x})^2}\right)^3}$$

for $x_i \in x$, where $\bar{x}$ is the sample mean.

Movement trajectories were measured using a lever affixed to a rotary encoder (US Digital) with a 60mm radius and 1250 pulses per revolution. Encoder values were collected at 1000 Hz, and trajectories were calculated by up-sampling at 200 μs (5000 Hz) using nearest-neighbor interpolation. Pulse number was converted to degrees, and the vertical displacement in millimeters was calculated using the chord length of the leaver displacement angle. 20-80% rise times were calculated using normalized average trajectories. Presses and releases were sorted according to duration in a window from 200ms before threshold crossing to the time of a threshold crossing half way between the top and bottom of the total lever displacement.

Wide-field imaging: Imaging analysis were performed using custom MATLAB code. Regions of interest (ROIs) were selected within empirically defined arm movement region of lobule simplex according to the spread of GCaMP expression. Window location and the lobule identity were identified according to folia patterns visible through the cranial window, landmarks recorded during surgery, and post-hoc histology. Baseline fluorescence (F) was measured on a trial-by-trial basis during the inter-trial interval (ITI) as the mean fluorescence 900 to 200ms before trial initiation. Normalized fluorescence (ΔF/F) was calculated according to the cumulative activity within an ROI, or on a pixel by pixel basis. Lever hold times <200ms in total or > 1 s after the visual cue were rare, and thus excluded from analysis. Lever releases between 175 and 1000ms following the visual cue were classified as correct, and releases prior to visual cue were classified as early. Lever releases ≤200 ms following the visual cue were considered too fast to be reactions to the cue based on average reaction time distributions. Peak ΔF/F was measured in the time window from 100ms before to 400 ms after lever release.

Meta K-means analysis: Images were first registered to reduce motion artifacts, and then thresholded at 70% of maximum intensity for each frame to remove background noise. Images were downsampled 5-fold in both X and Y. Baseline F was defined as the averaged fluorescence across the entire movie for each pixel, and used to normalize change in fluorescence (ΔF/F). ΔF/F was then re-normalized to the maximum ΔF/F during the entire movie for each pixel. The repeated

712 k-means clustering algorithm (meta-k-means) separated pixels to cluster centroids based on a
713 pairwise correlation distance function using Pearson's linear correlation coefficient (r). The final
714 clusters were determined by first thresholding all the k-means results at 800 out of 1000 runs, and
715 then by merging highly correlated clusters based on Dunn's index. Clusters occupying less than
716 3% of the total imaging field were excluded from further analysis. Intra-cluster and inter-cluster
717 correlation coefficients were calculated between 100 ms before and 300 ms after lever release
718 for both correct and early trials. To test for differences in the relationship between spike rates and
719 correlation coefficients between trial types, paired clusters from each distribution were resampled
720 with replacement and fit with a line to measure the y-intercept 1000 times. Statistical significance
721 was computed according to the 95% confidence interval of the distribution of y-intercept difference
722 values (difference between y-intercepts 0.0375 ± 0.0013, 95% confidence interval [0.0349,
723 0.0402]).
724
725 *Two-photon imaging*: Motion in the XY plane was corrected by sub-pixel image registration. To
726 isolate signals from individual PC dendrites, we utilized principal component analysis (PCA)
727 followed by independent component analysis (ICA). Final dendrite segmentation was achieved
728 by thresholding the smoothed spatial filters from ICA. A binary mask was created by combining
729 highly correlated pixels (correlation coefficient > 0.8) and removing any overlapped regions
730 between segmented dendrites. Fluorescence changes (ΔF) were normalized to a window of
731 baseline fluorescence (F) between 500ms and 100ms preceding trial initiation. Responses were
732 categorized as significant ($p<0.05$) according to a two-tailed t-test if the $\Delta F/F$ in a 200 ms window
733 surrounding lever press or release was statistically different from a 500 ms window immediately
734 preceding lever movement. To extract events on single trials used for estimation of complex spike
735 rates and event amplitudes, the first derivative of the raw fluorescence trace was thresholded at
736 2.5 standard deviations from baseline. Notably, image segmentation using these criteria did not
737 extract PC soma, which were clearly visible in many single- and two-photon imaging experiments.
738 For single trial amplitude measurements, only events well separated in time (greater than 650ms
739 from the next event) were considered; however, for measurements of rates, all events separated
740 by at least one frame were included.
741
742 *Additional statistics and data sharing*: Data are presented as mean ± s.e.m., unless stated
743 otherwise. Statistical tests were two-sided, and analyses of variance (ANOVA) were performed
744 when more than two groups were tested. Differences were considered statistically significant
745 when $P < 0.05$. No correction for multiple comparisons was applied. No statistical methods were
746 used to predetermine sample sizes. Data collection and analysis were not performed blind to the
747 conditions of the experiments, but data collection relied on automatized measurements and

subsequent analysis was based on code uniformly applied across experimental conditions. Data analysis code are available on GitHub (access available upon request). The data that support the findings of this study are available from the corresponding author upon reasonable request.

References

1. Albus, J.S. A theory of cerebellar function. *Mathematical Biosciences* **10**, 25-61 (1971).
2. Ito, M. Neural design of the cerebellar motor control system. *Brain Res* **40**, 81-84 (1972).
3. Marr, D. A theory of cerebellar cortex. *J Physiol* **202**, 437-470 (1969).
4. Ito, M., Sakurai, M. & Tongroach, P. Climbing fibre induced depression of both mossy fibre responsiveness and glutamate sensitivity of cerebellar Purkinje cells. *J Physiol* **324**, 113-134 (1982).
5. Ekerot, C.F. & Kano, M. Long-term depression of parallel fibre synapses following stimulation of climbing fibres. *Brain Res* **342**, 357-360 (1985).
6. Sakurai, M. Synaptic modification of parallel fibre-Purkinje cell transmission in in vitro guinea-pig cerebellar slices. *J Physiol* **394**, 463-480 (1987).
7. Miyakawa, H., Lev-Ram, V., Lasser-Ross, N. & Ross, W.N. Calcium transients evoked by climbing fiber and parallel fiber synaptic inputs in guinea pig cerebellar Purkinje neurons. *J Neurophysiol* **68**, 1178-1189 (1992).
8. Tank, D.W., Sugimori, M., Connor, J.A. & Llinas, R.R. Spatially resolved calcium dynamics of mammalian Purkinje cells in cerebellar slice. *Science* **242**, 773-777 (1988).
9. Konnerth, A., Dreessen, J. & Augustine, G.J. Brief dendritic calcium signals initiate long-lasting synaptic depression in cerebellar Purkinje cells. *Proc Natl Acad Sci U S A* **89**, 7051-7055 (1992).
10. Llinas, R. & Sugimori, M. electrophysiological properties of in vitro purkinje cell somata in mammalian cerebellar slices. *J. Physiol.*, 171-195 (1980).
11. Eccles, J.C., Llinas, R. & Sasaki, K. The excitatory synaptic action of climbing fibres on the Purkinje cells of the cerebellum. *J Physiol* **182**, 268-296 (1966).
12. Medina, J.F., Nores, W.L., Ohyama, T. & Mauk, M.D. Mechanisms of cerebellar learning suggested by eyelid conditioning. *Current opinion in neurobiology* **10**, 717-724 (2000).

779 13. Ohyama, T.N.W.M.M. & Mauk, M. What the cerebellum computes. *Trends in*
780 *Neurosciences* **26**, 222-227 (2003).
781 14. Raymond, J.L., Lisberger, S.G. & Mauk, M.D. The cerebellum: a neuronal learning
782 machine? *Science* **272**, 1126-1131 (1996).
783 15. Manto, M.*, et al.* Consensus paper: roles of the cerebellum in motor control--the diversity
784 of ideas on cerebellar involvement in movement. *Cerebellum* **11**, 457-487 (2012).
785 16. Schultz, S.R., Kitamura, K., Post-Uiterweer, A., Krupic, J. & Hausser, M. Spatial pattern
786 coding of sensory information by climbing fiber-evoked calcium signals in networks of
787 neighboring cerebellar Purkinje cells. *J Neurosci* **29**, 8005-8015 (2009).
788 17. Tsutsumi, S.*, et al.* Structure-function relationships between aldolase C/zebrin II
789 expression and complex spike synchrony in the cerebellum. *J Neurosci* **35**, 843-852 (2015).
790 18. Ozden, I., Dombeck, D.A., Hoogland, T.M., Tank, D.W. & Wang, S.S. Widespread state-
791 dependent shifts in cerebellar activity in locomoting mice. *PLoS One* **7**, e42650 (2012).
792 19. De Gruijl, J.R., Hoogland, T.M. & De Zeeuw, C.I. Behavioral correlates of complex spike
793 synchrony in cerebellar microzones. *J Neurosci* **34**, 8937-8947 (2014).
794 20. Tang, T., Suh, C.Y., Blenkinsop, T.A. & Lang, E.J. Synchrony is Key: Complex Spike Inhibition
795 of the Deep Cerebellar Nuclei. *Cerebellum* **15**, 10-13 (2016).
796 21. Lee, K.H.*, et al.* Circuit mechanisms underlying motor memory formation in the
797 cerebellum. *Neuron* **86**, 529-540 (2015).
798 22. Histed, M.H., Carvalho, L.A. & Maunsell, J.H. Psychophysical measurement of contrast
799 sensitivity in the behaving mouse. *J Neurophysiol* **107**, 758-765 (2012).
800 23. Schneiderman, N. & Gormezano, I. Conditioning of the Nictitating Membrane of the
801 Rabbit as a Function of Cs-Us Interval. *J Comp Physiol Psychol* **57**, 188-195 (1964).
802 24. Gaffield, M.A., Amat, S.B., Bito, H. & Christie, J.M. Chronic imaging of movement-related
803 Purkinje cell calcium activity in awake behaving mice. *J Neurophysiol* **115**, 413-422 (2016).
804 25. Mukamel, E.A., Nimmerjahn, A. & Schnitzer, M.J. Automated analysis of cellular signals
805 from large-scale calcium imaging data. *Neuron* **63**, 747-760 (2009).
806 26. Najafi, F., Giovannucci, A., Wang, S.S. & Medina, J.F. Coding of stimulus strength via analog
807 calcium signals in Purkinje cell dendrites of awake mice. *Elife* **3**, e03663 (2014).

808 27. Ozden, I., Lee, H.M., Sullivan, M.R. & Wang, S.S. Identification and clustering of event
809 patterns from in vivo multiphoton optical recordings of neuronal ensembles. *J Neurophysiol* **100**,
810 495-503 (2008).
811 28. Ozden, I., Sullivan, M.R., Lee, H.M. & Wang, S.S. Reliable coding emerges from
812 coactivation of climbing fibers in microbands of cerebellar Purkinje neurons. *J Neurosci* **29**,
813 10463-10473 (2009).
814 29. Najafi, F., Giovannucci, A., Wang, S.S. & Medina, J.F. Sensory-driven enhancement of
815 calcium signals in individual Purkinje cell dendrites of awake mice. *Cell Rep* **6**, 792-798 (2014).
816 30. Yang, Y. & Lisberger, S.G. Purkinje-cell plasticity and cerebellar motor learning are graded
817 by complex-spike duration. *Nature* **510**, 529-532 (2014).
818 31. Rudolph, S., Overstreet-Wadiche, L. & Wadiche, J.I. Desynchronization of multivesicular
819 release enhances Purkinje cell output. *Neuron* **70**, 991-1004 (2011).
820 32. Maruta, J., Hensbroek, R.A. & Simpson, J.I. Intraburst and interburst signaling by climbing
821 fibers. *J Neurosci* **27**, 11263-11270 (2007).
822 33. Kitamura, K. & Hausser, M. Dendritic calcium signaling triggered by spontaneous and
823 sensory-evoked climbing fiber input to cerebellar Purkinje cells in vivo. *J Neurosci* **31**, 10847-
824 10858 (2011).
825 34. Brenowitz, S.D. & Regehr, W.G. Associative short-term synaptic plasticity mediated by
826 endocannabinoids. *Neuron* **45**, 419-431 (2005).
827 35. Eilers, J., Augustine, G.J. & Konnerth, A. Subthreshold synaptic Ca2+ signalling in fine
828 dendrites and spines of cerebellar Purkinje neurons. *Nature* **373**, 155-158 (1995).
829 36. Hartell, N.A. Strong activation of parallel fibers produces localized calcium transients and
830 a form of LTD that spreads to distant synapses. *Neuron* **16**, 601-610 (1996).
831 37. Wang, S.S., Denk, W. & Hausser, M. Coincidence detection in single dendritic spines
832 mediated by calcium release. *Nat Neurosci* **3**, 1266-1273 (2000).
833 38. Andersson, G. & Oscarsson, O. Climbing fiber microzones in cerebellar vermis and their
834 projection to different groups of cells in the lateral vestibular nucleus. *Exp Brain Res* **32**, 565-579
835 (1978).
836 39. Apps, R. & Garwicz, M. Anatomical and physiological foundations of cerebellar
837 information processing. *Nat Rev Neurosci* **6**, 297-311 (2005).

838 40. Apps, R. Movement-related gating of climbing fibre input to cerebellar cortical zones.
839 *Prog Neurobiol* **57**, 537-562 (1999).
840 41. Horn, K.M., Van Kan, P.L. & Gibson, A.R. Reduction of rostral dorsal accessory olive
841 responses during reaching. *J Neurophysiol* **76**, 4140-4151 (1996).
842 42. Gellman, R., Gibson, A.R. & Houk, J.C. Inferior olivary neurons in the awake cat: detection
843 of contact and passive body displacement. *J Neurophysiol* **54**, 40-60 (1985).
844 43. Lawrenson, C.L., Watson, T.C. & Apps, R. Transmission of Predictable Sensory Signals to
845 the Cerebellum via Climbing Fiber Pathways Is Gated during Exploratory Behavior. *J Neurosci* **36**,
846 7841-7851 (2016).
847 44. Apps, R. & Lee, S. Gating of transmission in climbing fibre paths to cerebellar cortical C1
848 and C3 zones in the rostral paramedian lobule during locomotion in the cat. *J Physiol* **516 (Pt 3)**,
849 875-883 (1999).
850 45. Lidierth, M. & Apps, R. Gating in the spino-olivocerebellar pathways to the c1 zone of the
851 cerebellar cortex during locomotion in the cat. *J Physiol* **430**, 453-469 (1990).
852 46. Bengtsson, F. & Hesslow, G. Cerebellar control of the inferior olive. *Cerebellum* **5**, 7-14
853 (2006).
854 47. Horn, K.M., Hamm, T.M. & Gibson, A.R. Red nucleus stimulation inhibits within the inferior
855 olive. *J Neurophysiol* **80**, 3127-3136 (1998).
856 48. Weiss, C., Houk, J.C. & Gibson, A.R. Inhibition of sensory responses of cat inferior olive
857 neurons produced by stimulation of red nucleus. *J Neurophysiol* **64**, 1170-1185 (1990).
858 49. Bell, C.C. & Kawasaki, T. Relations among climbing fiber responses of nearby Purkinje
859 Cells. *J Neurophysiol* **35**, 155-169 (1972).
860 50. Sasaki, K., Bower, J.M. & Llinas, R. Multiple Purkinje Cell Recording in Rodent Cerebellar
861 Cortex. *Eur J Neurosci* **1**, 572-586 (1989).
862 51. Sugihara, I., Marshall, S.P. & Lang, E.J. Relationship of complex spike synchrony bands and
863 climbing fiber projection determined by reference to aldolase C compartments in crus IIa of the
864 rat cerebellar cortex. *J Comp Neurol* **501**, 13-29 (2007).
865 52. Sugihara, I. & Shinoda, Y. Molecular, topographic, and functional organization of the
866 cerebellar cortex: a study with combined aldolase C and olivocerebellar labeling. *J Neurosci* **24**,
867 8771-8785 (2004).

868 53. Sugihara, I., Wu, H.S. & Shinoda, Y. The entire trajectories of single olivocerebellar axons
869 in the cerebellar cortex and their contribution to Cerebellar compartmentalization. *J Neurosci* **21**,
870 7715-7723 (2001).
871 54. Voogd, J., Pardoe, J., Ruigrok, T.J. & Apps, R. The distribution of climbing and mossy fiber
872 collateral branches from the copula pyramidis and the paramedian lobule: congruence of
873 climbing fiber cortical zones and the pattern of zebrin banding within the rat cerebellum. *J*
874 *Neurosci* **23**, 4645-4656 (2003).
875 55. Ekerot, C.F., Garwicz, M. & Schouenborg, J. Topography and nociceptive receptive fields
876 of climbing fibres projecting to the cerebellar anterior lobe in the cat. *J Physiol* **441**, 257-274
877 (1991).
878 56. Oberdick, J., Baader, S.L. & Schilling, K. From zebra stripes to postal zones: deciphering
879 patterns of gene expression in the cerebellum. *Trends Neurosci* **21**, 383-390 (1998).
880 57. Hashimoto, M. & Mikoshiba, K. Mediolateral compartmentalization of the cerebellum is
881 determined on the "birth date" of Purkinje cells. *J Neurosci* **23**, 11342-11351 (2003).
882 58. Sarna, J.R., Marzban, H., Watanabe, M. & Hawkes, R. Complementary stripes of
883 phospholipase Cbeta3 and Cbeta4 expression by Purkinje cell subsets in the mouse cerebellum.
884 *J Comp Neurol* **496**, 303-313 (2006).
885 59. Sugihara, I. & Quy, P.N. Identification of aldolase C compartments in the mouse cerebellar
886 cortex by olivocerebellar labeling. *J Comp Neurol* **500**, 1076-1092 (2007).
887 60. Wang, X., Chen, G., Gao, W. & Ebner, T.J. Parasagittally aligned, mGluR1-dependent
888 patches are evoked at long latencies by parallel fiber stimulation in the mouse cerebellar cortex
889 in vivo. *J Neurophysiol* **105**, 1732-1746 (2011).
890 61. Zhou, H.*, et al.* Cerebellar modules operate at different frequencies. *Elife* **3**, e02536
891 (2014).
892 62. Paukert, M., Huang, Y.H., Tanaka, K., Rothstein, J.D. & Bergles, D.E. Zones of enhanced
893 glutamate release from climbing fibers in the mammalian cerebellum. *J Neurosci* **30**, 7290-7299
894 (2010).
895 63. De Zeeuw, C.I.*, et al.* Spatiotemporal firing patterns in the cerebellum. *Nat Rev Neurosci*
896 **12**, 327-344 (2011).
897 64. Blenkinsop, T.A. & Lang, E.J. Synaptic action of the olivocerebellar system on cerebellar
898 nuclear spike activity. *J Neurosci* **31**, 14708-14720 (2011).

899 65. Bengtsson, F., Ekerot, C.F. & Jorntell, H. In vivo analysis of inhibitory synaptic inputs and
900 rebounds in deep cerebellar nuclear neurons. *PLoS One* **6**, e18822 (2011).
901 66. Person, A.L. & Raman, I.M. Purkinje neuron synchrony elicits time-locked spiking in the
902 cerebellar nuclei. *Nature* **481**, 502-505 (2012).
903 67. McElvain, L.E., Bagnall, M.W., Sakatos, A. & du Lac, S. Bidirectional plasticity gated by
904 hyperpolarization controls the gain of postsynaptic firing responses at central vestibular nerve
905 synapses. *Neuron* **68**, 763-775 (2010).
906 68. Pugh, J.R. & Raman, I.M. Potentiation of mossy fiber EPSCs in the cerebellar nuclei by
907 NMDA receptor activation followed by postinhibitory rebound current. *Neuron* **51**, 113-123
908 (2006).
909 69. Miles, F.A. & Lisberger, S.G. Plasticity in the vestibulo-ocular reflex: a new hypothesis.
910 *Annu Rev Neurosci* **4**, 273-299 (1981).
911 70. Ohmae, S. & Medina, J.F. Climbing fibers encode a temporal-difference prediction error
912 during cerebellar learning in mice. *Nat Neurosci* **18**, 1798-1803 (2015).
913 71. de Solages, C.*, et al.* High-frequency organization and synchrony of activity in the purkinje
914 cell layer of the cerebellum. *Neuron* **58**, 775-788 (2008).
915

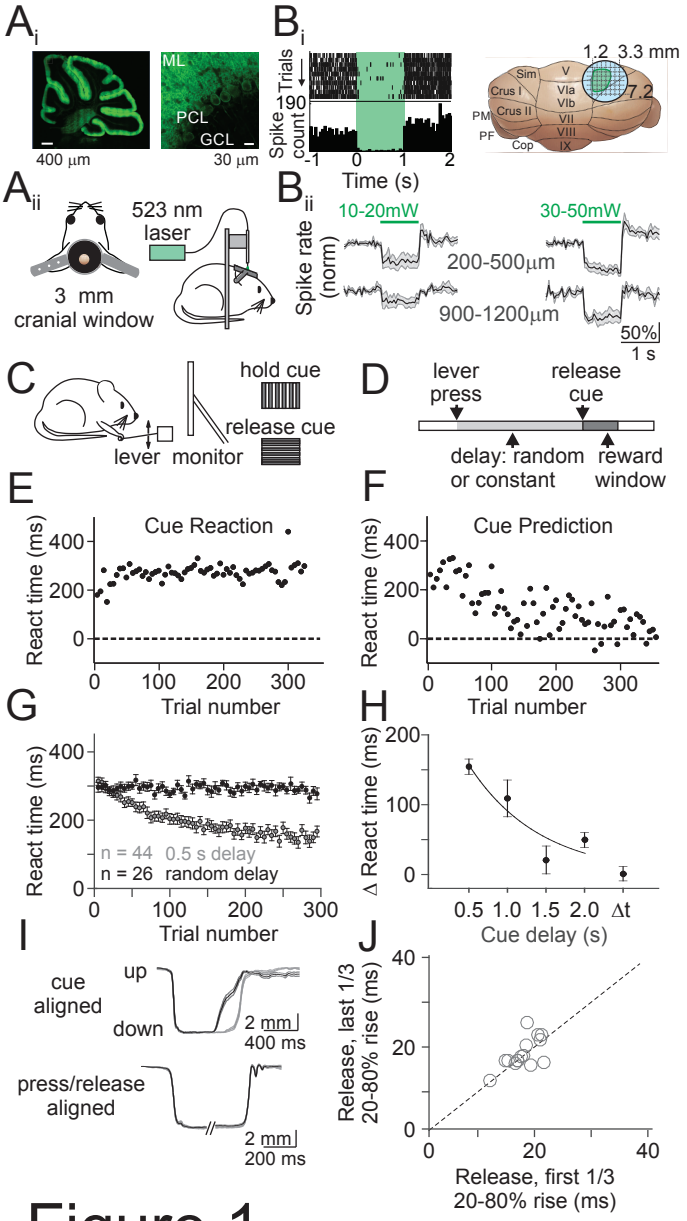
A_i
ML
PCL
GCL
400 µm
30 µm
B_i
Trials
190
Spike count
-1
0
1
2
Time (s)
1.2
3.3 mm
7.2
Sim
V
Crus I
VIa
VIb
Crus II
PM
VII
PF
VIII
Cop
IX
A_ii
523 nm laser
3 mm cranial window
B_ii
10-20mW
30-50mW
Spike rate (norm)
200-500µm
900-1200µm
50%
1 s
C
hold cue
release cue
lever
monitor
D
lever press
release cue
delay: random or constant
reward window
E
Cue Reaction
React time (ms)
400
200
0
0
100
200
300
Trial number
F
Cue Prediction
React time (ms)
400
200
0
0
100
200
300
Trial number
G
React time (ms)
400
200
0
n = 44 0.5 s delay
n = 26 random delay
0
100
200
300
Trial number
H
Δ React time (ms)
200
100
0
0.5
1.0
1.5
2.0
Δt
Cue delay (s)
I
cue aligned
up
down
2 mm
400 ms
press/release aligned
2 mm
200 ms
J
Release, last 1/3 20-80% rise (ms)
40
20
0
0
20
40
Release, first 1/3 20-80% rise (ms)

Figure 1

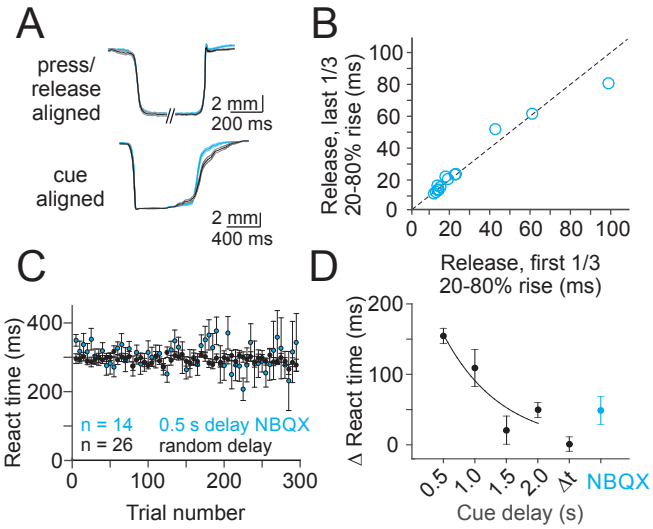
A
press/
release
aligned
2 mm
200 ms
cue
aligned
2 mm
400 ms
B
Release, last 1/3
20-80% rise (ms)
Release, first 1/3
20-80% rise (ms)
C
React time (ms)
n = 14
n = 26
0.5 s delay NBQX
random delay
Trial number
D
Δ React time (ms)
0.5
1.0
1.5
2.0
Δt
NBQX
Cue delay (s)

Figure 2

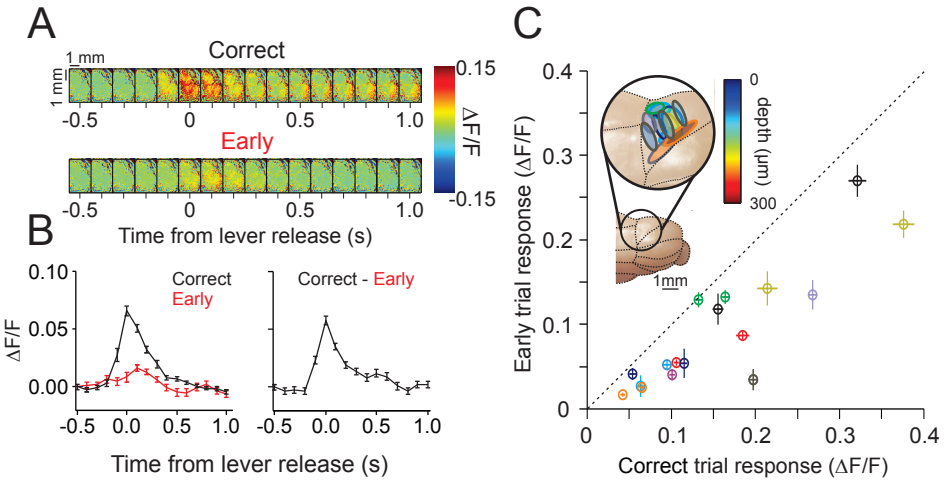
A
Correct
1 mm
1 mm
-0.5
0
0.5
1.0
Early
-0.5
0
0.5
1.0
Time from lever release (s)
0.15
ΔF/F
-0.15
B
0.10
0.05
0.00
ΔF/F
Correct
Early
Correct - Early
-0.5
0.0
0.5
1.0
-0.5
0.0
0.5
1.0
Time from lever release (s)
C
0.4
0.3
0.2
0.1
0
Early trial response (ΔF/F)
0
0.1
0.2
0.3
0.4
Correct trial response (ΔF/F)
0
depth (μm)
300
1mm

Figure 3

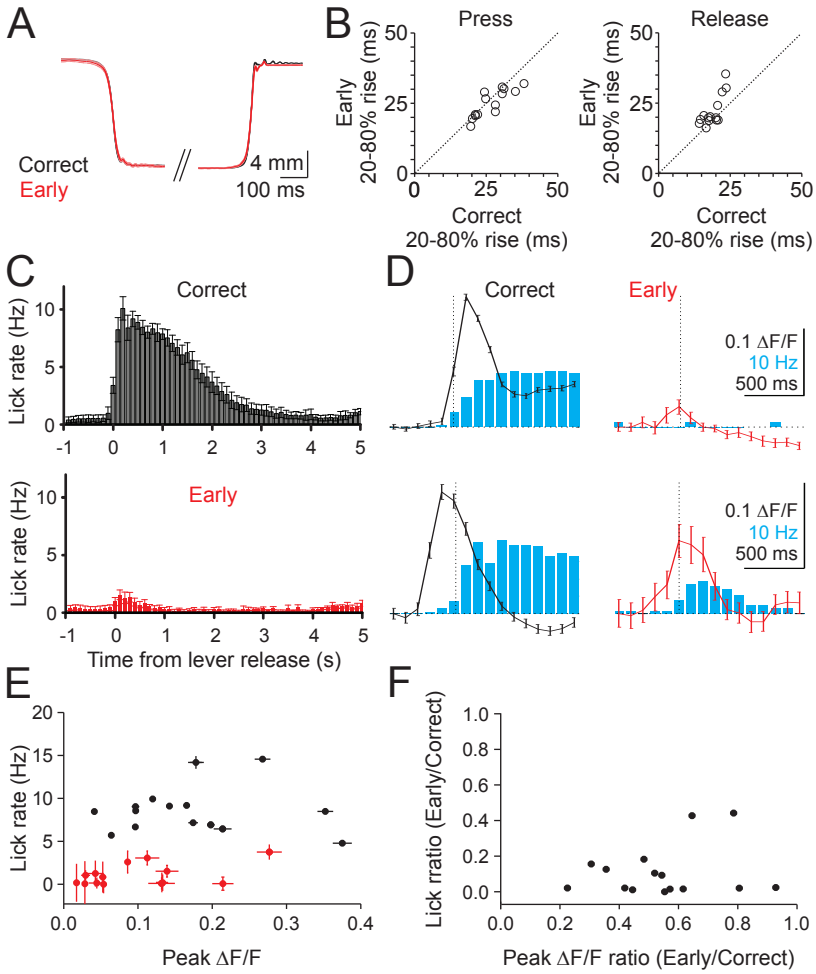
A
Correct
Early
4 mm
100 ms
B
Press
Release
Early 20-80% rise (ms)
Correct 20-80% rise (ms)
C
Correct
Early
Lick rate (Hz)
Time from lever release (s)
D
Correct
Early
0.1 ΔF/F
10 Hz
500 ms
E
Lick rate (Hz)
Peak ΔF/F
F
Lick rratio (Early/Correct)
Peak ΔF/F ratio (Early/Correct)

Figure 4

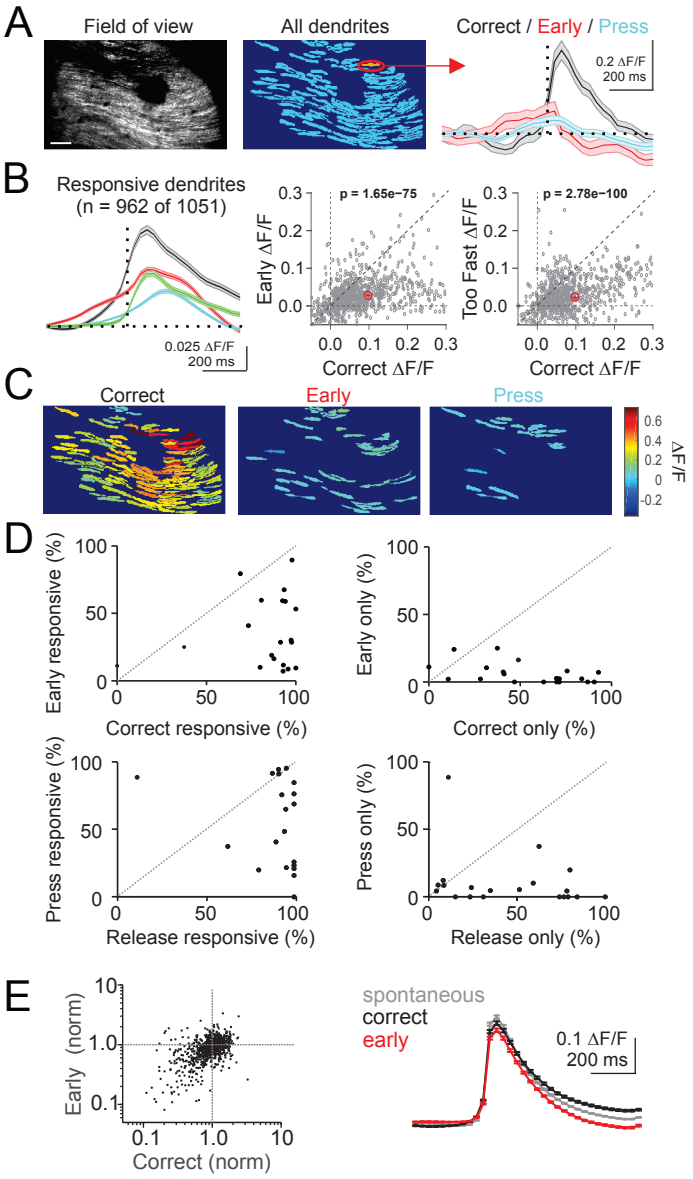
A
Field of view
All dendrites
Correct / Early / Press
0.2 ΔF/F
200 ms
B
Responsive dendrites
(n = 962 of 1051)
0.025 ΔF/F
200 ms
p = 1.65e−75
Early ΔF/F
Correct ΔF/F
p = 2.78e−100
Too Fast ΔF/F
Correct ΔF/F
C
Correct
Early
Press
ΔF/F
D
Early responsive (%)
Correct responsive (%)
Early only (%)
Correct only (%)
Press responsive (%)
Release responsive (%)
Press only (%)
Release only (%)
E
Early (norm)
Correct (norm)
spontaneous
correct
early
0.1 ΔF/F
200 ms

Figure 5

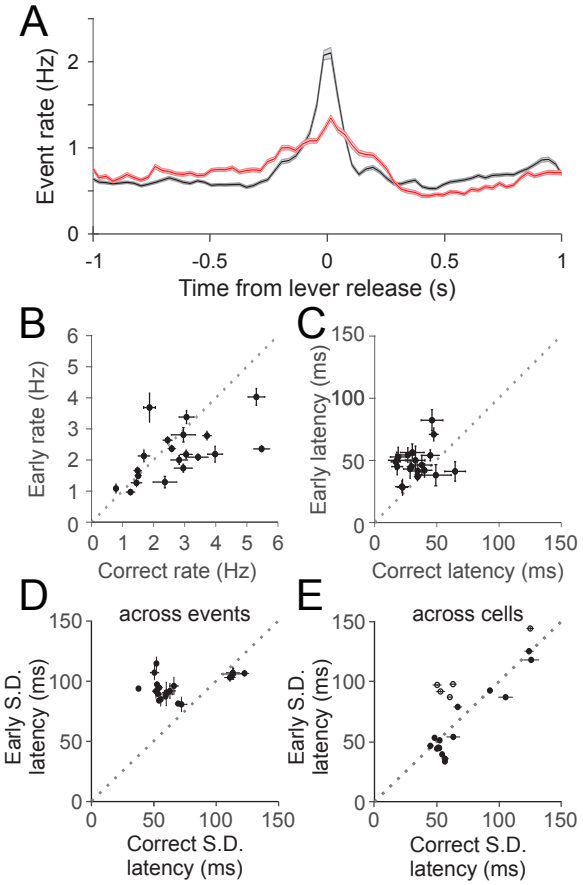
A
Event rate (Hz)
Time from lever release (s)
B
Early rate (Hz)
Correct rate (Hz)
C
Early latency (ms)
Correct latency (ms)
D
across events
Early S.D. latency (ms)
Correct S.D. latency (ms)
E
across cells
Early S.D. latency (ms)
Correct S.D. latency (ms)

Figure 6

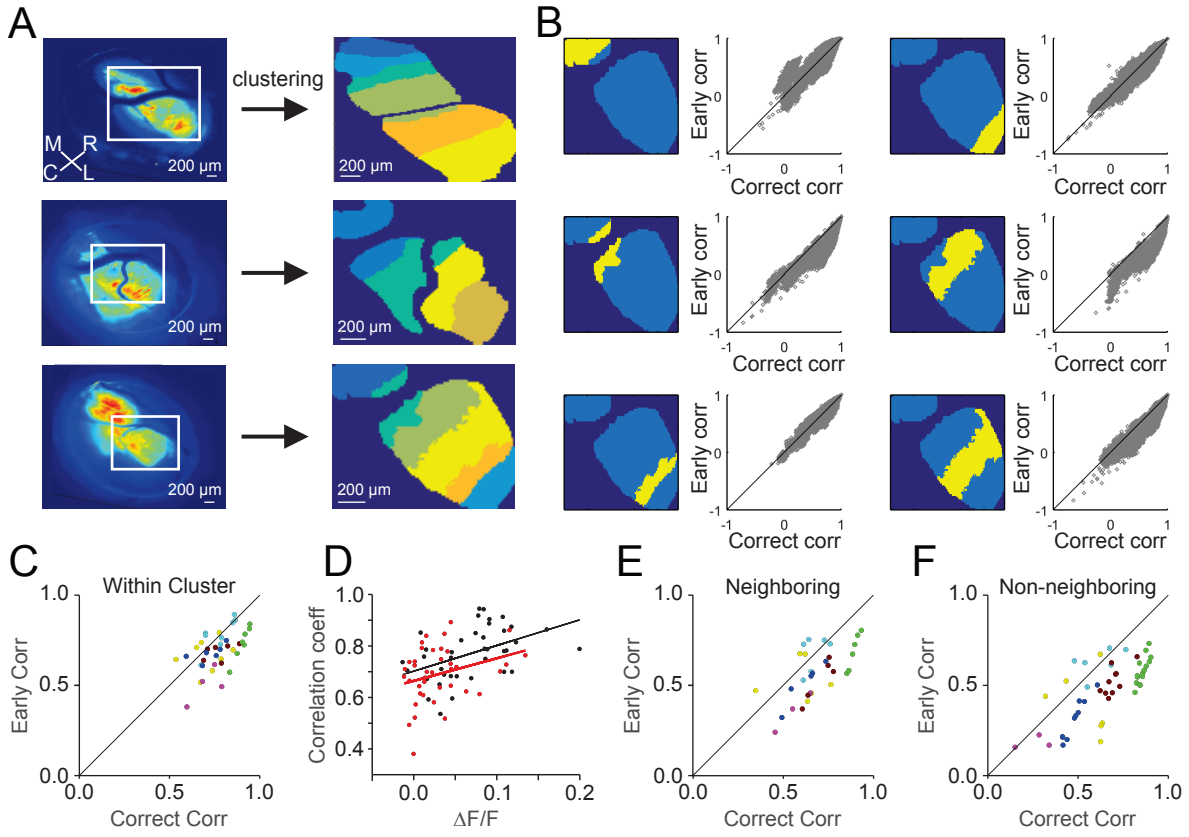
A
clustering
M
R
C
L
200 µm
B
Early corr
Correct corr
C
Within Cluster
Early Corr
Correct Corr
D
Correlation coeff
ΔF/F
E
Neighboring
F
Non-neighboring

Figure 7

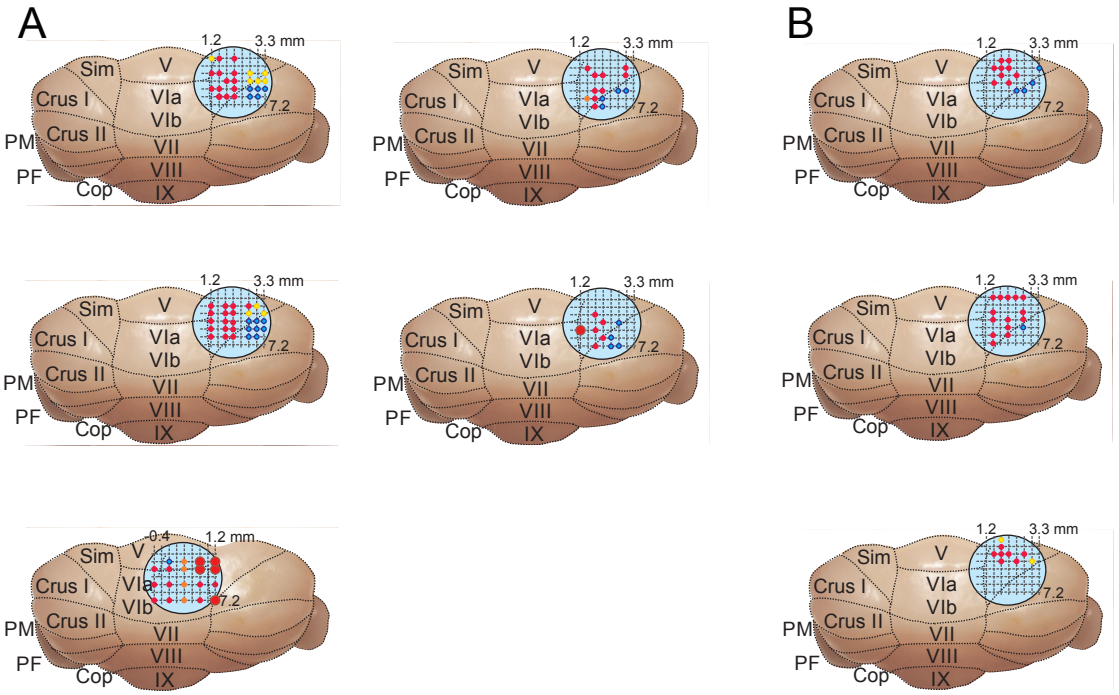

Arch: 5 mice
10-50mW, one Step pulse for 1sec

Right arm
Right & Left arms
Very weak arm movements
Whiskers or mouth or nose
nothing

Electrical Stim. 3 mice
0.1mA-1mA
50Hz for 500ms or 1sec

Right arm
Right & Left arms
Very weak arm movements
Whiskers or mouth or nose
nothing

supplemental figure 1

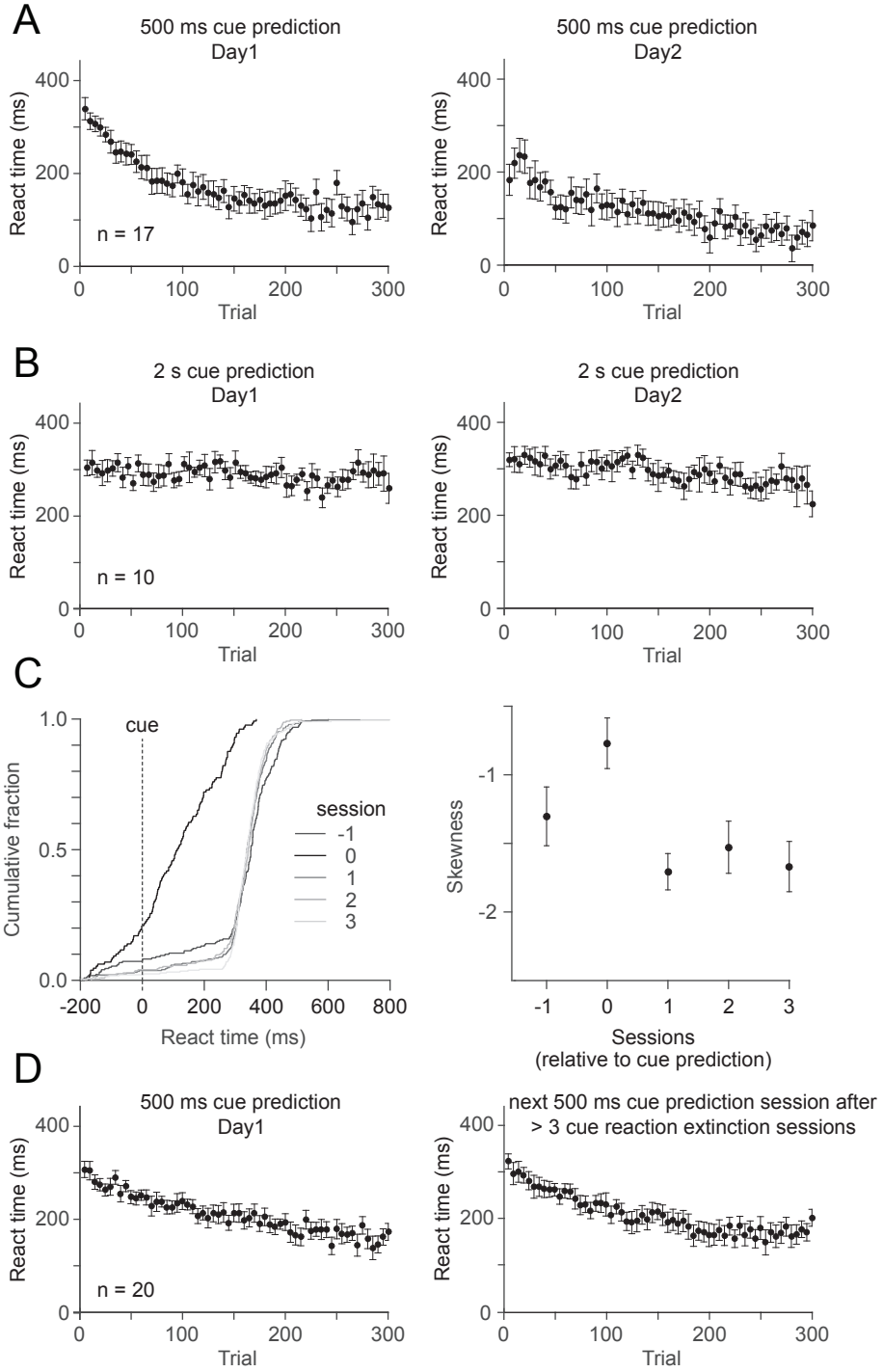

supplemental figure 2

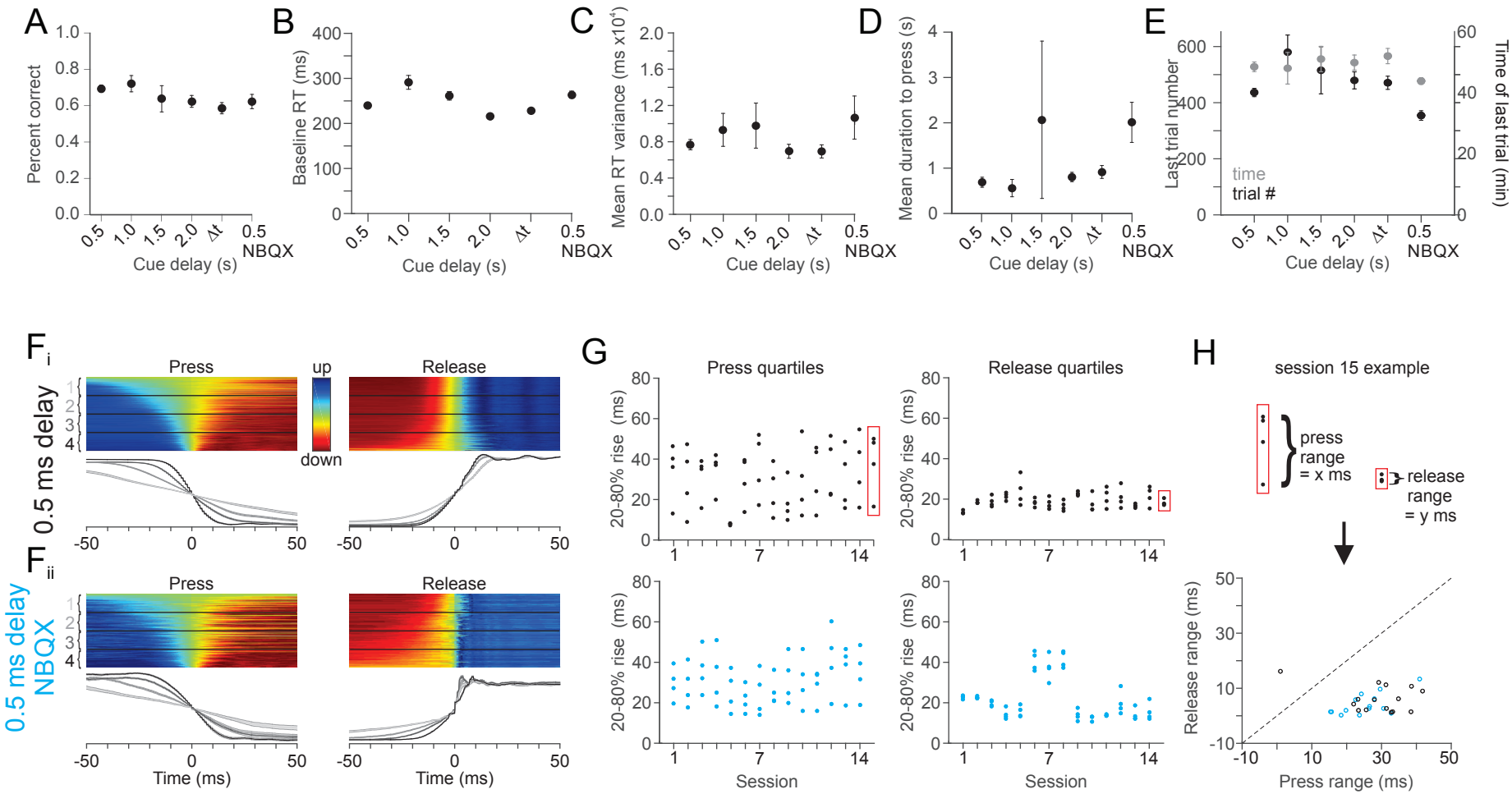

supplemental figure 3

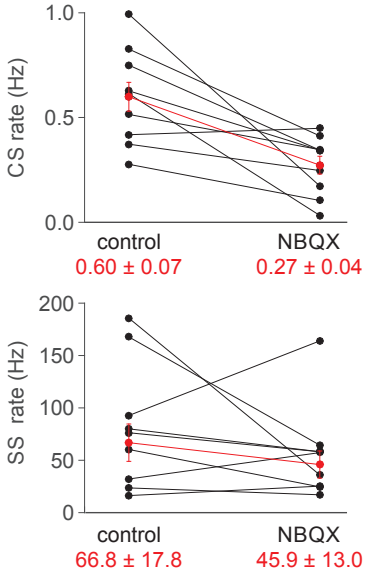

supplemental figure 4

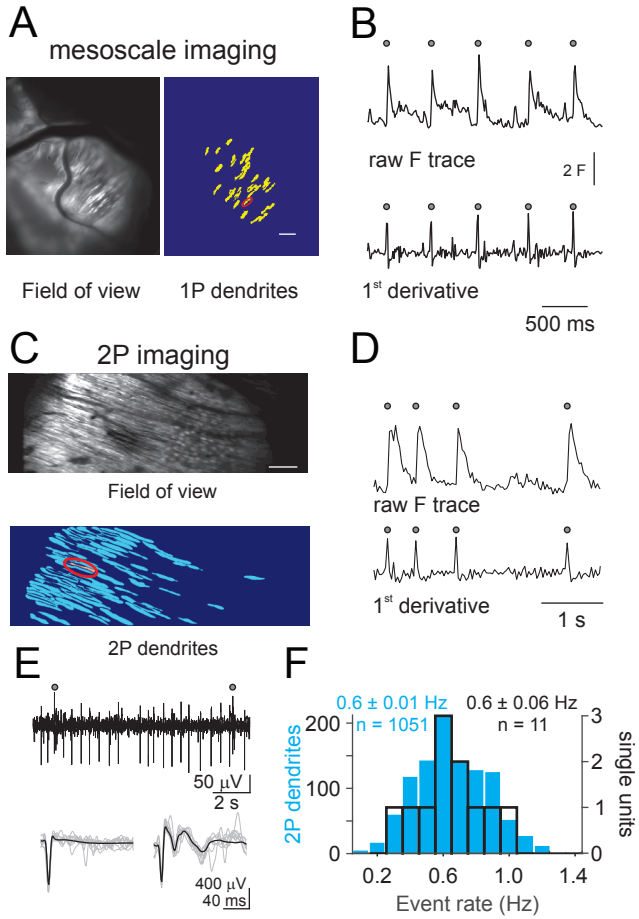

supplemental figure 5